Nano Research 2017, 10(11): 3875–3884
DOI 10.1007/s12274-017-1601-8
Research Article

ISSN 1998-0124
CN 11-5974/O4

Quasi-freestanding, striped WS_2 monolayer with an invariable band gap on Au(001)

Min Hong[1,2], Xiebo Zhou[1,2], Jianping Shi[1,2], Yue Qi[2], Zhepeng Zhang[1,2], Qiyi Fang[1,2], Yaguang Guo[1], Yajuan Sun[3], Zhongfan Liu[2], Yuanchang Li[4], Qian Wang[1,5], and Yanfeng Zhang[1,2] (✉)

[1] *Department of Materials Science and Engineering, College of Engineering, Peking University, Beijing 100871, China*
[2] *Center for Nanochemistry (CNC), Beijing National Laboratory for Molecular Sciences, College of Chemistry and Molecular Engineering, Academy for Advanced Interdisciplinary Studies, Peking University, Beijing 100871, China*
[3] *State Key Laboratory of Coal-based Low-carbon Energy, ENN Group Co., Ltd., Langfang 065001, China*
[4] *National Center for Nanoscience and Technology, Chinese Academy of Sciences, Beijing 100190, China*
[5] *Center for Applied Physics and Technology, Peking University, Beijing 100871, China*

Received: 16 January 2017
Revised: 11 March 2017
Accepted: 19 March 2017

KEYWORDS

WS_2,
Au(001),
striped superstructure,
interfacial interaction,
STM/STS

ABSTRACT

Revealing the structural/electronic features and interfacial interactions of monolayer MoS_2 and WS_2 on metals is essential to evaluating the performance of related devices. In this study, we focused on the atomic-scale features of monolayer WS_2 on Au(001) synthesized via chemical vapor deposition. Scanning tunneling microscopy and spectroscopy reveal that the WS_2/Au(001) system exhibits a striped superstructure similar to that of MoS_2/Au(001) but weaker interfacial interactions, as evidenced by experimental and theoretical investigations. Specifically, the WS_2/Au(001) band gap exhibits a relatively intrinsic value of ~ 2.0 eV. However, the band gap can gradually decrease to ~ 1.5 eV when the sample annealing temperature increases from ~ 370 to 720 °C. In addition, the doping level (or Fermi energy) of monolayer WS_2/Au(001) varies little over the valley and ridge regions of the striped patterns because of the homogenous distributions of point defects introduced by annealing. Briefly, this work provides an in-depth investigation into the interfacial interactions and electronic properties of monolayer MX_2 on metal substrates.

1 Introduction

Recently, two-dimensional transition metal dichalcogenides, specifically MX_2 (M = Mo, W; X = S, Se, etc.), have attracted significant interest due to their abundant, intriguing electronic and optical properties [1–3]. For example, unlike semimetal graphene with a zero band gap, monolayer MX_2 usually acts as a semiconductor with an electronic band gap in the visible spectral range [4]. In addition, indirect-to-direct band gap transitions in the monolayer regime [5–7], strong photovoltaic responses [8, 9], and interesting valley-related physics

Address correspondence to yanfengzhang@pku.edu.cn

[10] endow monolayer MX_2 with significant potential for use in electronic and optoelectronic devices [11, 12].

The most intriguing property of monolayer MX_2 is the tunability of its electronic structures. According to published reports, its band gap was tunable with layer thickness [5, 13–16], structural defects [17–20], strain effects [21–23], etc. Moreover, the spatially varying interlayer coupling induced by the Moiré patterns in MX_2-based heterostructures have been theoretically predicted to localize the valence band maximum (VBM) state [24]. Recently, Zhang et al. experimentally observed variations in interlayer coupling in MoS_2/WSe_2 hetero-bilayers, and quantitatively demonstrated how interlayer coupling affects the electronic structure at different critical points [25].

The contact interfaces between monolayer MX_2 and metal electrodes are never negligible in electronic devices. Thus, the interfacial interactions between monolayer MX_2 and metallic substrates and the effect of metal substrates on the electronic properties of monolayer MX_2 are fundamental issues worth examining. Sørensen et al. demonstrated the presence of strong interfacial interactions between monolayer MoS_2 and Au(111) and attributed the decrease in the gap value and the modification of the band gap edges to the Au donor states [26]. Shi et al. also measured a reduced band gap for MoS_2 grown on Au foil via chemical vapor deposition (CVD) [27]. However, the interfacial interactions weakened dramatically when monolayer graphene was placed between MoS_2 and the Au substrate, leading to a more intrinsic band gap. Moreover, monolayer MoS_2 on Au(001) was reported to exhibit a new periodically striped superstructure pattern [28]. The doping level of MoS_2 was modulated periodically by the striped superstructures. In this regard, the electronic properties or band gaps of MX_2 on metals largely depend on the interfacial coupling strength.

Monolayer WS_2 is another important member of the two-dimensional MX_2 class of materials. Although monolayer WS_2 has been successfully synthesized on Au foil via low- and atmospheric-pressure CVD methods [29–31], the interfacial interactions and electronic properties of WS_2/Au have not been reported thus far.

In this work, we reveal the atomic-scale features and quasiparticle band gap of CVD-grown monolayer WS_2 on Au foil via high-resolution scanning tunneling microscopy and spectroscopy (STM/STS). The results of this study are complementary or comparable to those from MoS_2 on Au(001), which exhibits a striped superstructure pattern and a significantly reduced band gap. The samples were exposed to a high-temperature annealing process to generate point defects and to allow examination of the spatial distributions of the defects over the valley and ridge regions of the striped superstructures, thus addressing the homogenous or inhomogeneous interactions of WS_2/Au(001). Moreover, theoretical calculations were performed to determine the different interfacial binding energies of monolayer WS_2/Au(001) and MoS_2/Au(001), and to confirm their different interfacial interactions.

2 Results and discussion

Traditional low-pressure CVD (LPCVD) was used to directly synthesize WS_2 on Au foil based on a previously reported method [31]. The corresponding scanning electron microscopy (SEM) image in Fig. 1(a) indicates deposition of a random distribution of triangular WS_2 flakes with an average edge length of ~ 300 nm on the Au substrate. X-ray photoelectron spectroscopy (XPS) (Fig. 1(b) and Fig. S1 in the Electronic Supplementary Material (ESM)) was used to confirm WS_2 formation. The W 4f and S 2p peak positions are consistent with previously reported WS_2 data [32, 33]. Moreover, Raman measurements were performed to identify the layer thicknesses of the as-grown samples (Fig. 1(c)). Two typical Raman peaks, which correspond to the E^1_{2g} and A_{1g} phonon modes centered at ~ 356.8 and 419.9 cm^{-1}, respectively, were observed with a frequency difference (Δ) of ~ 63.2 cm^{-1}. This frequency difference confirms that WS_2 was deposited as a monolayer [31, 34, 35].

To analyze the atomic-scale morphologies and electronic properties of WS_2/Au foil, low-temperature STM/STS (~ 78 K) characterizations were performed on the as-grown samples. Prior to STM measurements, the CVD samples were annealed at ~ 370 °C for 2 h in an ultra-high vacuum (UHV) system to remove adsorbed impurities. A unique striped superstructure with a periodicity of ~ 4.78 ± 0.13 nm was obtained,

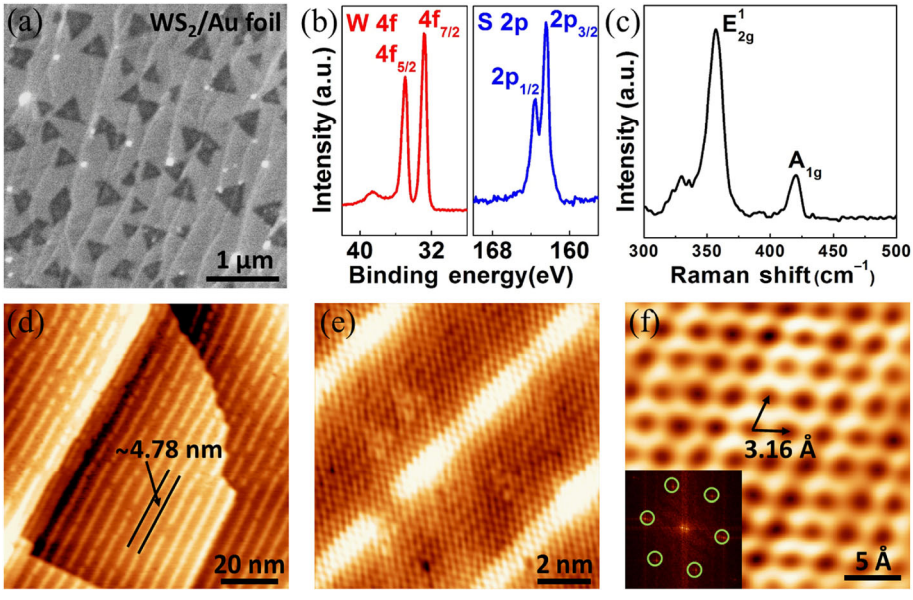

Figure 1 Morphological and spectroscopic characterizations of monolayer WS_2 on Au foil synthesized via LPCVD. (a) SEM image of WS_2 triangles on the Au foil substrate. (b) and (c) XPS and Raman spectra of the as-grown WS_2/Au samples. (d) Large-scale STM image (V_{Sample} = 1.80 V, $I_{Tunneling}$ = 0.56 nA; 100 nm × 100 nm) of WS_2 on Au(001) after annealing at ~ 370 °C for 2 h. The period of the striped superstructures is indicated to be ~ 4.78 ± 0.13 nm. (e) Atomically resolved STM image (1.20 V, 0.51 nA; 15 nm × 15 nm) of the striped superstructures. (f) Zoom-in STM image of the WS_2 honeycomb lattice (0.002 V, 9.80 nA; 4 nm × 4 nm). Inset: the corresponding FFT pattern.

as shown in the large-scale STM image in Fig. 1(d). This striped superstructure resembles the previously reported striped pattern formed in MoS_2/Au(001) [28]. The striped pattern is thought to form because of the symmetry difference and lattice mismatch between MoS_2 and Au(001) [28]. Accordingly, the striped superstructure observed here is thought to originate from the same reason, i.e., the spreading of the WS_2 lattice on the Au(001) facet.

Interestingly, the striped pattern can extend over the different Au(001) terraces, and large-area coherence can be noted within the WS_2 lattice. To confirm this result, Figs. 1(e) and 1(f) show sequential zoom-in STM images of the striped patterns. A honeycomb lattice with an interatomic distance of ~ 3.16 Å is visible, which is consistent with previous reports on the WS_2 lattice [34]. The relatively high crystal quality of CVD-grown WS_2 on Au(001) is also indicated by the presence of only one set of hexagonally arranged 2D fast Fourier transform (FFT) spots (inset of Fig. 1(f)).

Hexagonally shaped moiré patterns are commonly observed in all three-fold symmetry systems such as MoS_2/Au(111) [26, 36] and graphene/hexagonal boron nitride (h-BN) [37]. However, striped superstructure patterns formed in systems with hexagonal overlayer stacking on rectangular substrates (e.g., WS_2/Au(001) or MoS_2/Au(001) [28]) have rarely been reported. Figure 2(a) is a three-dimensional STM image of typical WS_2 striped superstructures on the Au(001) facet, where the CVD samples underwent a mild annealing process at ~ 370 °C for 2 h. The periodicity of ~ 4.78 ± 0.13 nm between adjacent stripes and corrugation of ~ 0.15 ± 0.01 nm over the ridge and valley regions can be deduced from the corresponding line profile below the image. Further magnification of this region in Fig. 2(b) reveals the aligned orientations of the WS_2 atomic rows (black arrow) and striped superstructures (blue arrow). Notably, this alignment is universally present in a large-area random scan of the samples, suggesting the uniform orientation of WS_2 with regard to the Au(100) facet.

Based on the perfect alignment between the WS_2 lattice and the striped superstructure, the specific stacking geometries of WS_2 on Au(001) and the resulting superstructure were simulated using spherical models. As shown in Fig. 2(c), monolayer WS_2 is stacked on the (1 × 1) square lattice of Au(001) ($a_{Au(001)}$ = 0.288 nm) with almost no relative rotation (highlighted by

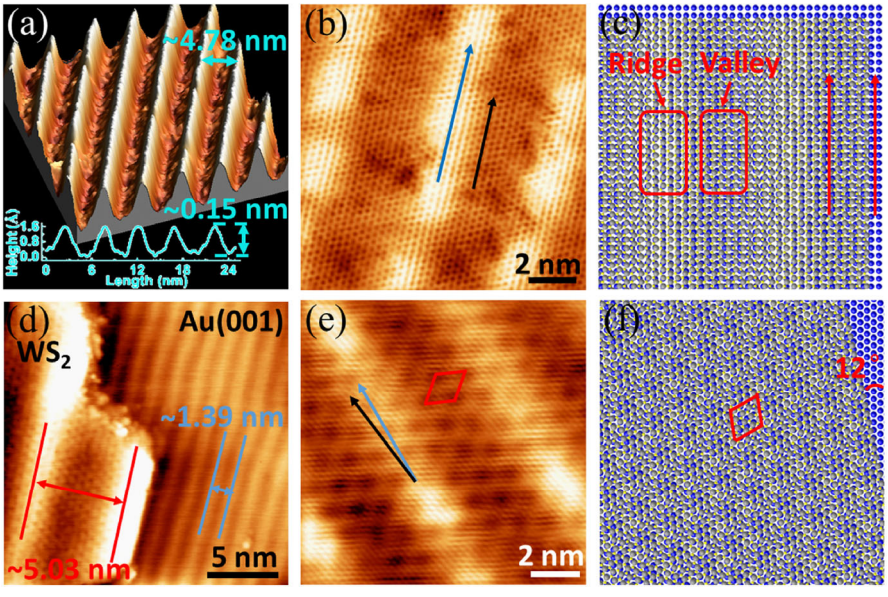

Figure 2 STM characterizations and structural simulations of striped superstructures in WS_2/Au(001) after different annealing processes. (a) Three-dimensional (3D) STM image (2.50 V, 200 pA; 30 nm × 30 nm) of WS_2 striped superstructures after annealing at ~ 370 °C for 2 h, indicating a period of ~ 4.78 ± 0.13 nm between the adjacent stripes. The inserted line profile reveals a corrugation of ~ 0.15 ± 0.01 nm. (b) Atomically resolved STM image (1.00 V, 0.53 nA; 12 nm × 12 nm) of the striped superstructures. The orientations of the superstructure stripe and atomic row of WS_2 are indicated by the blue and black arrows, respectively. (c) Simulation of the striped superstructure of monolayer WS_2 stacking on the (1 × 1) square lattice of Au(001). (d) and (e) STM images (0.70 V, 0.60 nA, 20 nm × 20 nm and 1.37 V, 3.23 nA, 12 nm × 12 nm) of the "composite superstructure" formed by WS_2/Au(001) after annealing at ~ 820 °C for 1 h. (f) Simulation of the evolved hexagonal moiré patterns formed by monolayer WS_2 stacking on the hex-reconstructed Au(001) lattice.

red arrows). If the lattice constant of WS_2 (3.16 Å) is allowed to contract only slightly (by ~ 0.6%) to 3.14 Å, the resulting period of the simulated stripes becomes ~ 4.88 nm. This simulated result is clearly consistent with the universally observed patterns that exhibit a period of ~ 4.78 ± 0.13 nm. Moreover, the ridge and valley regions (labeled by red frames) in Fig. 2(c) exhibit different placements of W and S atoms on the Au(001) lattice. That is, the S atoms are placed on top of the Au atoms in the bright ridge regions, while both W and S atoms are positioned on the Au hollow sites in the dark valley regions. The region dependence of the metal and S atom locations should cause periodic surface undulations and varying adlayer-substrate interactions, as previously reported of MoS_2 on Au substrates [26, 28]. The different symmetries and the mismatch between the WS_2 and Au(001) lattices should induce the formation of striped superstructures.

However, the situation changed significantly after the WS_2/Au sample underwent high-temperature annealing at ~ 820 °C for 1 h in the UHV chamber. As shown in Fig. 2(d), two types of striped patterns with different periods emerge simultaneously. In the right portion of the image (labeled with blue lines), a pattern with a periodicity of ~ 1.39 ± 0.04 nm is obtained, and is consistent with the previously reported hex-reconstruction of Au(001) [38]. This pattern appears because the top-layer Au(001) atoms rearrange into a contracted quasihexagonal lattice on the bulk (1 × 1) square lattice after being annealed in the UHV system, leading to the formation of striped patterns [38, 39].

Another type of striped pattern is observed in the left portion of the image (labeled with red lines in Fig. 2(d)), which is thought to be WS_2 on Au(001). However, the striped pattern has a larger periodicity (~ 5.03 ± 0.55 nm) than that evolved from the mild annealing process (4.78 ± 0.13 nm in Fig. 2(a)). More intriguingly, a new type of hexagonal moiré pattern is superimposed on the WS_2 striped pattern (Figs. 2(d) and 2(e)), and constitutes a "composite superstructure". Thus far, the most reasonable explanation for this composite superstructure is stacking of WS_2 on the hex-reconstructed Au(001) facet. As shown in the simulated patterns in Fig. 2(f), the monolayer WS_2

lattice is stacked on the hex-reconstructed layer, i.e., the hexagonal lattice of hex-Au(001) ($a_{\text{hex-Au(001)}}$ = 0.277 nm), with a relative rotation angle of 12°. A hexagonal moiré pattern is generated in the simulation, and its periodicity (~ 1.21 nm) is in line with the experimental data (~ 1.26 nm in Fig. 2(e)). Considering the (1 × 1) square lattice of bulk Au(001) and the surface hex-reconstruction, the coexistence of striped and hexagonal patterns of WS_2 on hex-Au(001) is reasonable. However, further theoretical analysis and simulation are required to clarify the formation mechanism and structural model of this "composite superstructure" pattern.

In this regard, the annealing temperature is a critical factor in the transformation of the superstructure shape/composition in the WS_2/Au(001) system. Note that, this "composite superstructure" was not observed in a similar MoS_2/Au(001) system [28], even after high-temperature annealing. Based on previous experimental results, the MoS_2 layer was expected to lift the surface reconstruction of Au(001) due to the relatively high binding force between MoS_2 and the Au(001) facet [28]. In contrast, the binding force between WS_2 and the Au(001) facet appears much weaker, and thus the hex-reconstructed Au(001) layer was preserved between WS_2 and the bulk Au(001) atoms.

The morphologies, band gaps, and interfacial binding forces of WS_2/Au(001) and MoS_2/Au(001) were also compared. Figures 3(a) and 3(b) show STM images of the striped patterns formed in the two systems. A mild annealing process (~ 370 °C for 2 h under UHV conditions) was applied to the sample before STM imaging. Analogous striped superstructures forming by MX_2 resting on Au(001) are clearly visible. However, different superstructure periodicities and surface undulations can be distinguished from the corresponding height profiles in Fig. 3(c). The WS_2/Au(001) system has a periodicity of ~ 4.78 ± 0.13 nm and a corrugation of ~ 0.15 ± 0.01 nm between the ridge and valley regions, whereas the corresponding values for MoS_2/Au(001) are ~ 8.00 ± 0.41 nm and ~ 0.25 nm [28], respectively. The relatively small surface undulation in WS_2/Au(001) suggests that its interfacial interactions are weaker than those of MoS_2/Au(001).

To verify this, density functional theory (DFT) calculations were performed to estimate the binding energies of WS_2 and MoS_2 on Au(001). The supercells selected for the calculations are shown in Figs. 3(d) and 3(e), and are constructed from the $(11\times\sqrt{3})$ overlayer on (11 × 2) Au(001). The resulting binding energies of WS_2 and MoS_2 are 36.4 and 46.6 meV per transition metal atom, respectively. MoS_2 clearly binds much more strongly onto Au(001) than WS_2, which proves that the interfacial interactions between WS_2 and Au(001) are weaker than those between MoS_2 and Au(001). Notably, different interfacial-interaction-induced surface undulations were also reported for other two-dimensional layered materials on metal substrates, e.g., graphene and h-BN on Rh(111) [40] and Ir(111) [41], based on both experimental results and theoretical calculations.

The STS spectrum of WS_2/Au(001) was compared to that of MoS_2/Au(001), and their different band gaps were examined (Fig. 3(f)). In detail, six spectra obtained at different positions within the ridge regions overlap one another and exhibit nearly identical band gaps. The VBM and conduction band minimum (CBM) of monolayer MoS_2 on Au(001) (upper spectra in Fig. 3(f)) are located at ~ −1.20 and +0.30 V, respectively, indicating a quasiparticle band gap (E_g) of ~ 1.50 eV with an apparent n-doping effect. The observed E_g is apparently lower than that reported for a graphite substrate (~ 2.40 eV) [16]. This difference is thought to be a result of the strong interfacial interaction between MoS_2 and Au(001) and electron donation from the Au substrate to MoS_2 [28].

In contrast, the VBM and CBM of WS_2 on Au(001) (lower spectra in Fig. 3(f)) are located at ~ −1.20 and +0.80 V, respectively, yielding an E_g of ~ 2.00 eV with a slight n-doping effect. This gap is close to the previous STS result for WS_2 on quartz coated by a gold film (2.38 eV) [42]. In addition, the band gaps in the valleys exhibit the same features as those of the ridges in both systems (Fig. S2 in the ESM). Consequently, WS_2 on Au(001) maintains a more intrinsic band gap than MoS_2. This result should serve as another direct indication that the interfacial interactions of WS_2/Au(001) are weaker than those of MoS_2/Au(001).

Point defects in MoS_2 such as sulfur vacancies have been reported as possible reasons for its n-doping effect [19, 43, 44]. Recently, the distribution of point

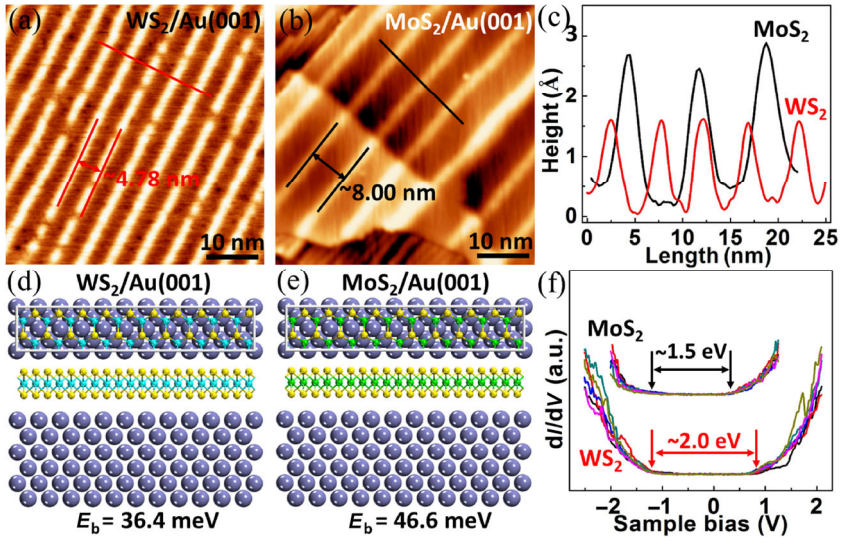

Figure 3 Comparisons of the morphologies and band gaps of similar striped WS_2/Au(001) and MoS_2/Au(001) patterns, as well as the DFT calculations of the binding energies (E_b) of the two systems. The CVD-derived samples were annealed at ~ 370 °C for 2 h before STM imaging. (a) and (b) Large-scale STM images (3.00 V, 200 pA, 50 nm × 50 nm and 0.80 V, 300 pA, 50 nm × 50 nm) reveal similar striped patterns in WS_2/Au(001) and MoS_2/Au(001), respectively. (c) Corresponding height profiles of WS_2 and MoS_2 on Au(001) measured along the red and black lines in (a) and (b), respectively, showing the superstructure periodicity and surface corrugation of the two types of systems. (d) and (e) Top and side views of the supercells constructed from WS_2 and MoS_2 on Au(001) and used for DFT calculations. (f) STS spectra of MoS_2 and WS_2 (1.90 V, 400 pA, V_{rms} = 10 mV, f = 932 Hz and 2.50 V, 200 pA, 10 mV, 932 Hz) at six different positions in the ridge regions.

defects was reported to vary significantly between the ridge and valley regions of the striped patterns in MoS_2/Au(001), leading to tunable n-doping levels in the two types of regions [28]. This study also examines defect types and densities, as well as their effects on the electronic properties of WS_2/Au(001), since WS_2/Au(001) should interact more weakly than MoS_2/Au(001) in the valley and ridge regions. The WS_2/Au samples were processed at various annealing temperatures to generate defects in monolayer WS_2.

Figures 4(a)–4(c) show atomically resolved STM images of WS_2/Au(001) after annealing at ~ 370, 500, and 720 °C for 2 h, respectively. Typical striped superstructures and point defects appear in all WS_2/Au(001) images. The sequential zoom-in STM images in Figs. 4(d) and 4(e) identify these defects as single S-vacancies (V_s) (highlighted by blue arrows). Moreover, the WS_2 lattices and defects show different STM contrasts compared with those of the images shown in Fig. 2. This is probably induced by tip condition variation [17, 45].

Notably, the defect types shown in Figs. 4(a)–4(c) change little as the annealing temperature increases, although the defect density increases. To clarify this, defect density statistics were calculated for samples exposed to various annealing processes. The statistical results in Fig. 4(f) indicate that the WS_2/Au(001) defect densities in the ridge regions increase from 0.073 ± 0.019 to 0.308 ± 0.019 nm^{-2} when the annealing temperature increases from ~ 370 to 720 °C. Moreover, the defect densities in the valley regions are similar to those of the ridge regions under all circumstances. Thus, the overall defect densities increase as the annealing temperature increases, and the defects are always uniformly distributed between ridge and valley regions.

This defect distribution is distinctly different from that of MoS_2 on Au(001), where the defects evolve preferentially in the ridge regions of the MoS_2 striped patterns [28]. Based on the large surface undulation in MoS_2/Au(001) (~ 0.25 nm), an apparent undulation of the interfacial coupling strength between the ridge and valley regions is expected. This might induce a nonuniform distribution of defects in the two typical surface regions. In contrast, WS_2 on Au(001) exhibits a much smaller surface undulation (~ 0.15 nm), which

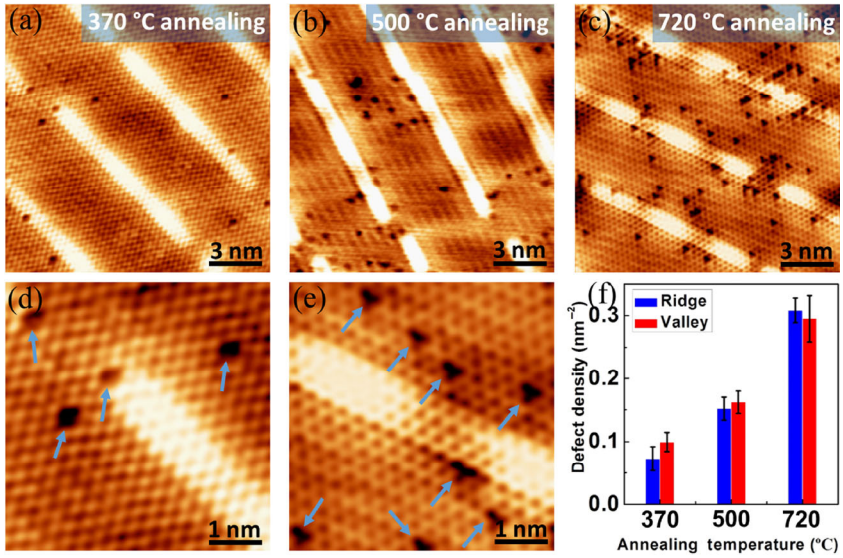

Figure 4 Defect density variations in WS_2/Au(001) after various annealing processes. (a)–(c) Atomically resolved STM images (0.20 V, 0.89 nA, 15 nm × 15 nm; 0.08 V, 0.95 nA, 15 nm × 15 nm; and 0.24 V, 0.84 nA, 15 nm × 15 nm) of monolayer WS_2 on Au(001) after annealing at ~ 370, 500, and 720 °C for 2 h, respectively. (d) and (e) Zoom-in STM images (0.20 V, 0.89 nA, 5 nm × 5 nm and 0.14 V, 0.60 nA, 5 nm × 5 nm) of the defects in (a) and (c), respectively. (f) Experimental statistics show the defect densities in the ridge and valley regions of the striped superstructures as a function of annealing temperature.

is in line with the nearly homogeneous adlayer-substrate interaction in the ridge/valley regions and ultimately a homogenous point defect distribution.

The influence of various annealing temperatures on the WS_2/Au(001) band gap was also determined from the STM/STS measurements. The images in Figs. 5(a) and 5(b) present typical morphologies of WS_2 striped patterns on Au(001) after annealing at ~ 370 and 720 °C, respectively. The lower STS spectra were obtained at the labeled positions of the corresponding samples. The configuration after annealing at ~ 500 °C is shown in Fig. S3 of the ESM for comparison. The STM image and corresponding STS spectra of MoS_2/Au(001) after annealing at ~ 720 °C are shown in Fig. 5(c). In each case, six spectra were captured at specific ridge and valley positions (labeled by colored points in the insets) along the vertical direction of the striped patterns to illustrate the variation and repeatability of the band gaps.

In the WS_2/Au(001) sample annealed at ~ 370 °C for 2 h (Fig. 5(a)), the VBM and CBM are located at ~ −1.20 and +0.80 V, respectively, and yield the previously mentioned relatively intrinsic band gap of ~ 2.00 eV with a small n-type doping effect. However, when the annealing temperature increases to ~ 720 °C (Fig. 5(b)), the locations of the VBM and CBM change to ~ −1.0 and +0.5 V, respectively, which decreases the band gap to ~ 1.50 eV and imparts a stronger n-doping effect. These phenomena are plausible for the following reasons. The high-temperature annealing process enhances interfacial interactions between WS_2 and Au substrate. The Au donor states and electron donation to the WS_2 layer from Au substrate are enhanced (see the XPS spectra of the annealed sample in Fig. S4 in the ESM). According to a previously published report [26], the Au donor states modify the band gap edges of MX_2 and cause an obvious band gap reduction. In addition, electron donation and increased defects should enhance the n-doping effect [19, 43, 44].

Moreover, after annealing at ~ 720 °C for 2 h, MoS_2/Au(001) exhibits a periodic Fermi level (doping level) shift, which is thought to result from its non-uniform defect distribution (Fig. 5(c)) [28]. In contrast, for WS_2/Au(001), the CBM and VBM positions in the ridges are always identical to those in the valleys. Namely, the Fermi level (doping level) changes little between these two typical regions regardless of the degree of annealing. Given the homogeneous distribution of point defects in the ridge and valley regions of the striped WS_2 patterns, the defect-derived n-doping

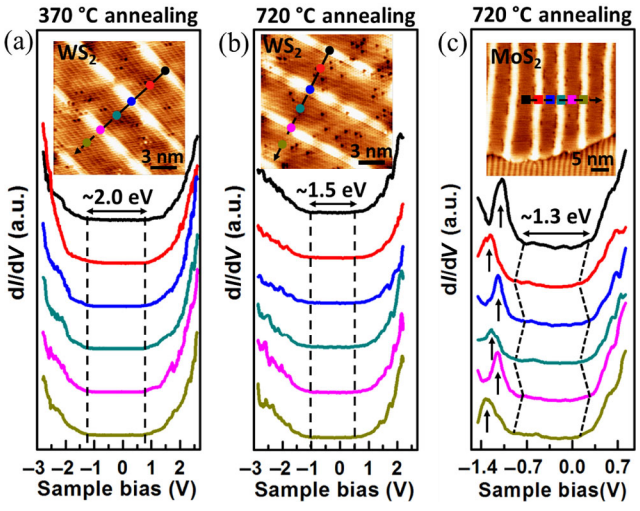

Figure 5 Band gap variations in WS_2/Au(001) and MoS_2/Au(001) after different annealing processes. (a) and (b) STM images (0.20 V, 940 pA, 15 nm × 15 nm and 0.20 V, 490 pA, 15 nm × 15 nm) of WS_2/Au(001) after annealing at ~ 370 and 720 °C for 2 h, respectively, and the corresponding STS spectra (2.50 V, 200 pA, 10 mV, 932 Hz and 2.50 V, 200 pA, 10 mV, 932 Hz) at the positions marked with colored dots (along the black arrow). (c) STM image (1.00 V, 200 pA, 30 nm × 30 nm) of MoS_2/Au(001) after annealing the sample at ~ 720 °C for 2 h and the corresponding STS spectra (1.00 V, 200 pA, 10 mV, 932 Hz) at the positions marked with colored squares (along the black arrow).

effects on these two types of regions are nearly equal, and lead to constant doping levels in the samples.

3 Conclusion

In summary, we have revealed the periodically striped superstructure of CVD-grown WS_2 on Au(001). The relatively weak interfacial interactions between WS_2 and Au(001) were confirmed using STM/STS characterization and DFT calculations, and verified via the nearly intrinsic quasiparticle band gap (~ 2.0 eV). Moreover, we find that the defect distributions are nearly homogenous over the ridge and valley regions of the WS_2 striped patterns regardless of the annealing process used. The position of the Fermi level in WS_2/Au(001) is the same in both ridge and valley regions, which contrasts sharply with the inhomogeneous distribution of defects and periodic modulations of the doping levels in MoS_2/Au(001). This work sheds light on periodic modulation of the morphologies and electronic properties of MX_2 materials via substrate reconstruction.

4 Experimental

4.1 WS_2 growth procedures

Monolayer WS_2 was grown on Au foil inside a multitemperature-zone tubular furnace (Lindberg/Blue M) that contained a quartz tube with a diameter of 1 in. Sulfur powder was placed outside the hot zone and mildly sublimated at ~ 103 °C. WO_3 powder (Alfa Aesar, purity 99.9%) and Au foil (Alfa Aesar, purity 99.985%, thickness ~ 25 μm) were placed successively inside the hot center. Ar (50 sccm) and H_2 (5 sccm) were used as carrier gases. The growth pressure and temperature were set to ~ 18 Pa and ~ 880 °C, respectively. The growth time was ~ 30 min.

4.2 Characterization

The samples were characterized via SEM (Hitachi S-4800, 1-5 kV), XPS (Kratos, Axis Ultra with Mg Kα), and Raman spectroscopy (Horiba, LabRAM HR-800, ~ 514 nm). A Unisoku LT-STM/STS system was used for STM characterization and STS measurements. The STS spectra were measured at ~ 78 K by recording the output of a lock-in system with its feedback loop manually disabled.

4.3 DFT calculations

First-principles calculations were performed using the projector augmented wave [46] method within the Perdew–Burke–Ernzerhof [47] generalized gradient approximation, as implemented in the Vienna *ab initio* simulation package (VASP) [48]. The slab model was used with a (11 × 2) Au (001) supercell to accommodate $(10\times\sqrt{3})$ MoS_2. A k mesh of 1 × 9 × 1 was used to sample the Brillouin zone. In the simulations, the bottommost three out of the six Au layers were fixed at their respective bulk positions while all other atoms were fully relaxed without any symmetry constraints until the residual forces were less than 0.03 eV/Å.

Acknowledgements

We acknowledge financial support by the National Natural Science Foundation of China (Nos. 51472008 and 51290272), the National Key Research and Development Program of China (No. 2016YFA0200103),

the Beijing Municipal Science and Technology Planning Project (No. Z151100003315013), the Open Research Fund Program of the State Key Laboratory of Low-Dimensional Quantum Physics (No. KF201601) and the ENN Energy Research Institute.

Electronic Supplementary Material: Supplementary material (further details of the XPS spectra, STM/STS measurements) is available in the online version of this article at https://doi.org/10.1007/s12274-017-1601-8.

References

[1] Chhowalla, M.; Shin, H. S.; Eda, G.; Li, L.-J.; Loh, K. P.; Zhang, H. The chemistry of two-dimensional layered transition metal dichalcogenide nanosheets. *Nat. Chem.* **2013**, *5*, 263–275.

[2] Wang, Q. H.; Kalantar-Zadeh, K.; Kis, A.; Coleman, J. N.; Strano, M. S. Electronics and optoelectronics of two-dimensional transition metal dichalcogenides. *Nat. Nanotechnol.* **2012**, *7*, 699–712.

[3] Butler, S. Z.; Hollen, S. M.; Cao, L. Y.; Cui, Y.; Gupta, J. A.; Gutiérrez, H. R.; Heinz, T. F.; Hong, S. S.; Huang, J. X.; Ismach, A. F. et al. Progress, challenges, and opportunities in two-dimensional materials beyond graphene. *ACS Nano* **2013**, *7*, 2898–2926.

[4] Xia, F. N.; Wang, H.; Xiao, D.; Dubey, M.; Ramasubramaniam, A. Two-dimensional material nanophotonics. *Nat. Photonics* **2014**, *8*, 899–907.

[5] Zhang, Y.; Chang, T.-R.; Zhou, B.; Cui, Y.-T.; Yan, H.; Liu, Z. K.; Schmitt, F.; Lee, J.; Moore, R.; Chen, Y. L. et al. Direct observation of the transition from indirect to direct bandgap in atomically thin epitaxial $MoSe_2$. *Nat. Nanotechnol.* **2014**, *9*, 111–115.

[6] Mak, K. F.; Lee, C. G.; Hone, J.; Shan, J.; Heinz, T. F. Atomically thin MoS_2: A new direct-gap semiconductor. *Phys. Rev. Lett.* **2010**, *105*, 136805.

[7] Splendiani, A.; Sun, L.; Zhang, Y. B.; Li, T. S.; Kim, J.; Chim, C.-Y.; Galli, G.; Wang, F. Emerging photoluminescence in monolayer MoS_2. *Nano Lett.* **2010**, *10*, 1271–1275.

[8] Bernardi, M.; Palummo, M.; Grossman, J. C. Extraordinary sunlight absorption and one nanometer thick photovoltaics using two-dimensional monolayer materials. *Nano Lett.* **2013**, *13*, 3664–3670.

[9] Britnell, L.; Ribeiro, R. M.; Eckmann, A.; Jalil, R.; Belle, B. D.; Mishchenko, A.; Kim, Y.-J.; Gorbachev, R. V.; Georgiou, T.; Morozov, S. V. et al. Strong light-matter interactions in heterostructures of atomically thin films. *Science* **2013**, *340*, 1311–1314.

[10] Xiao, D.; Liu, G.-B.; Feng, W. X.; Xu, X. D.; Yao, W. Coupled spin and valley physics in monolayers of MoS_2 and other group-VI dichalcogenides. *Phys. Rev. Lett.* **2012**, *108*, 196802.

[11] Radisavljevic, B.; Radenovic, A.; Brivio, J.; Giacometti, V.; Kis, A. Single-layer MoS_2 transistors. *Nat. Nanotechnol.* **2011**, *6*, 147–150.

[12] Lopez-Sanchez, O.; Lembke, D.; Kayci, M.; Radenovic, A.; Kis, A. Ultrasensitive photodetectors based on monolayer MoS_2. *Nat. Nanotechnol.* **2013**, *8*, 497–501.

[13] Jin, W. C.; Yeh, P.-C.; Zaki, N.; Zhang, D. T.; Sadowski, J. T.; Al-Mahboob, A.; van Der Zande, A. M.; Chenet, D. A.; Dadap, J. I.; Herman, I. P. et al. Direct measurement of the thickness-dependent electronic band structure of MoS_2 using angle-resolved photoemission spectroscopy. *Phys. Rev. Lett.* **2013**, *111*, 106801.

[14] Komsa, H.-P.; Krasheninnikov, A. V. Effects of confinement and environment on the electronic structure and exciton binding energy of MoS_2 from first principles. *Phys. Rev. B* **2012**, *86*, 241201.

[15] Kuc, A.; Zibouche, N.; Heine, T. Influence of quantum confinement on the electronic structure of the transition metal sulfide TS_2. *Phys. Rev. B* **2011**, *83*, 245213.

[16] Huang, Y. L.; Chen, Y. F.; Zhang, W. J.; Quek, S. Y.; Chen, C.-H.; Li, L.-J.; Hsu, W.-T.; Chang, W.-H.; Zheng, Y. J.; Chen, W. et al. Bandgap tunability at single-layer molybdenum disulphide grain boundaries. *Nat. Commun.* **2015**, *6*, 6298.

[17] Fuhr, J. D.; Saúl, A.; Sofo, J. O. Scanning tunneling microscopy chemical signature of point defects on the MoS_2(0001) surface. *Phys. Rev. Lett.* **2004**, *92*, 026802.

[18] Zou, X. L.; Liu, Y. Y.; Yakobson, B. I. Predicting dislocations and grain boundaries in two-dimensional metal-disulfides from the first principles. *Nano Lett.* **2013**, *13*, 253–258.

[19] Zhou, W.; Zou, X. L.; Najmaei, S.; Liu, Z.; Shi, Y. M.; Kong, J.; Lou, J.; Ajayan, P. M.; Yakobson, B. I.; Idrobo, J.-C. Intrinsic structural defects in monolayer molybdenum disulfide. *Nano Lett.* **2013**, *13*, 2615–2622.

[20] Yue, Q.; Chang, S. L.; Qin, S. Q.; Li, J. B. Functionalization of monolayer MoS_2 by substitutional doping: A first-principles study. *Phys. Lett. A* **2013**, *377*, 1362–1367.

[21] Castellanos-Gomez, A.; Roldán, R.; Cappelluti, E.; Buscema, M.; Guinea, F.; van der Zant, H. S. J.; Steele, G. A. Local strain engineering in atomically thin MoS_2. *Nano Lett.* **2013**, *13*, 5361–5366.

[22] Conley, H. J.; Wang, B.; Ziegler, J. I.; Haglund, R. F., Jr.; Pantelides, S. T.; Bolotin, K. I. Bandgap engineering of strained monolayer and bilayer MoS_2. *Nano Lett.* **2013**, *13*, 3626–3630.

[23] Feng, J.; Qian, X. F.; Huang, C.-W.; Li, J. Strain-engineered artificial atom as a broad-spectrum solar energy funnel. *Nat. Photonics* **2012**, *6*, 866–872.

[24] Kang, J.; Li, J. B.; Li, S.-S.; Xia, J.-B.; Wang, L.-W. Electronic structural moiré pattern effects on $MoS_2/MoSe_2$ 2D heterostructures. *Nano Lett.* **2013**, *13*, 5485–5490.

[25] Zhang, C. D.; Chuu, C. P.; Ren, X. B.; Li, M. Y.; Li, L.-J.; Jin, C. H.; Chou, M. Y.; Shih, C.-K. Interlayer couplings, moiré patterns, and 2D electronic superlattices in MoS_2/WSe_2 hetero-bilayers. *Sci. Adv.* **2017**, *3*, e1601459.

[26] Sørensen, S. G.; Füchtbauer, H. G.; Tuxen, A. K.; Walton, A. S.; Lauritsen, J. V. Structure and electronic properties of *in situ* synthesized single-layer MoS_2 on a gold surface. *ACS Nano* **2014**, *8*, 6788–6796.

[27] Shi, J. P.; Liu, M. X.; Wen, J. X.; Ren, X. B.; Zhou, X. B.; Ji, Q. Q.; Ma, D. L.; Zhang, Y.; Jin, C. H.; Chen, H. J. et al. All chemical vapor deposition synthesis and intrinsic bandgap observation of MoS_2/graphene heterostructures. *Adv. Mater.* **2015**, *27*, 7086–7092.

[28] Zhou, X. B.; Shi, J. P.; Qi, Y.; Liu, M. X.; Ma, D. L.; Zhang, Y.; Ji, Q. Q.; Zhang, Z. P.; Li, C.; Liu, Z. F. et al. Periodic modulation of the doping level in striped MoS_2 superstructures. *ACS Nano* **2016**, *10*, 3461–3468.

[29] Gao, Y.; Liu, Z. B.; Sun, D.-M.; Huang, L.; Ma, L.-P.; Yin, L.-C.; Ma, T.; Zhang, Z. Y.; Ma, X.-L.; Peng, L.-M. et al. Large-area synthesis of high-quality and uniform monolayer WS_2 on reusable Au foils. *Nat. Commun.* **2015**, *6*, 8569.

[30] Yun, S. J.; Chae, S. H.; Kim, H.; Park, J. C.; Park, J.-H.; Han, G. H.; Lee, J. S.; Kim, S. M.; Oh, H. M.; Seok, J. et al. Synthesis of centimeter-scale monolayer tungsten disulfide film on gold foils. *ACS Nano* **2015**, *9*, 5510–5519.

[31] Zhang, Y. S.; Shi, J. P.; Han, G. F.; Li, M. J.; Ji, Q. Q.; Ma, D. L.; Zhang, Y.; Li, C.; Lang, X. Y.; Zhang, Y. F. et al. Chemical vapor deposition of monolayer WS_2 nanosheets on Au foils toward direct application in hydrogen evolution. *Nano Res.* **2015**, *8*, 2881–2890.

[32] Cheng, L.; Huang, W. J.; Gong, Q. F.; Liu, C. H.; Liu, Z.; Li, Y. G.; Dai, H. J. Ultrathin WS_2 nanoflakes as a high-performance electrocatalyst for the hydrogen evolution reaction. *Angew. Chem., Int. Ed.* **2014**, *53*, 7860–7863.

[33] Zhang, Y.; Zhang, Y. F.; Ji, Q. Q.; Ju, J.; Yuan, H. T.; Shi, J. P.; Gao, T.; Ma, D. L.; Liu, M. X.; Chen, Y. B. et al. Controlled growth of high-quality monolayer WS_2 layers on sapphire and imaging its grain boundary. *ACS Nano* **2013**, *7*, 8963–8971.

[34] Gutiérrez, H. R.; Perea-López, N.; Elías, A. L.; Berkdemir, A.; Wang, B.; Lv, R. T.; López-Urías, F.; Crespi, V. H.; Terrones, H.; Terrones, M. Extraordinary room-temperature photoluminescence in triangular WS_2 monolayers. *Nano Lett.* **2013**, *13*, 3447–3454.

[35] Elías, A. L.; Perea-López, N.; Castro-Beltrán, A.; Berkdemir, A.; Lv, R. T.; Feng, S. M.; Long, A. D.; Hayashi, T.; Kim, Y. A.; Endo, M. et al. Controlled synthesis and transfer of large-area WS_2 sheets: From single layer to few layers. *ACS Nano* **2013**, *7*, 5235–5242.

[36] Krane, N.; Lotze, C.; Läger, J. M.; Reecht, G.; Franke, K. J. Electronic structure and luminescence of quasi-freestanding MoS_2 nanopatches on Au(111). *Nano Lett.* **2016**, *16*, 5163–5168.

[37] Yankowitz, M.; Xue, J. M.; Cormode, D.; Sanchez-Yamagishi, J. D.; Watanabe, K.; Taniguchi, T.; Jarillo-Herrero, P.; Jacquod, P.; LeRoy, B. J. Emergence of superlattice dirac points in graphene on hexagonal boron nitride. *Nat. Phys.* **2012**, *8*, 382–386.

[38] Hammer, R.; Sander, A.; Förster, S.; Kiel, M.; Meinel, K.; Widdra, W. Surface reconstruction of Au(001): High-resolution real-space and reciprocal-space inspection. *Phys. Rev. B* **2014**, *90*, 035446.

[39] Zhou, X. B.; Qi, Y.; Shi, J. P.; Niu, J. J.; Liu, M. X.; Zhang, G. H.; Li, Q. C.; Zhang, Z. P.; Hong, M.; Ji, Q. Q. et al. Modulating the electronic properties of monolayer graphene using a periodic quasi-one-dimensional potential generated by hex-reconstructed Au(001). *ACS Nano* **2016**, *10*, 7550–7557.

[40] Gao, Y. B.; Zhang, Y. F.; Chen, P. C.; Li, Y. C.; Liu, M. X.; Gao, T.; Ma, D. L.; Chen, Y. B.; Cheng, Z. H.; Qiu, X. H. et al. Toward single-layer uniform hexagonal boron nitride–graphene patchworks with zigzag linking edges. *Nano Lett.* **2013**, *13*, 3439–3443.

[41] Liu, M. X.; Li, Y. C.; Chen, P. C.; Sun, J. Y.; Ma, D. L.; Li, Q. C.; Gao, T.; Gao, Y. B.; Cheng, Z. H.; Qiu, X. H. et al. Quasi-freestanding monolayer heterostructure of graphene and hexagonal boron nitride on Ir(111) with a zigzag boundary. *Nano Lett.* **2014**, *14*, 6342–6347.

[42] Hill, H. M.; Rigosi, A. F.; Rim, K. T.; Flynn, G. W.; Heinz, T. F. Band alignment in MoS_2/WS_2 transition metal dichalcogenide heterostructures probed by scanning tunneling microscopy and spectroscopy. *Nano Lett.* **2016**, *16*, 4831–4837.

[43] Hong, J. H.; Hu, Z. X.; Probert, M.; Li, K.; Lv, D. H.; Yang, X. N.; Gu, L.; Mao, N. N.; Feng, Q. L.; Xie, L. M. et al. Exploring atomic defects in molybdenum disulphide monolayers. *Nat. Commun.* **2015**, *6*, 6293.

[44] Komsa, H.-P.; Kotakoski, J.; Kurasch, S.; Lehtinen, O.; Kaiser, U.; Krasheninnikov, A. V. Two-dimensional transition metal dichalcogenides under electron irradiation: Defect production and doping. *Phys. Rev. Lett.* **2012**, *109*, 035503.

[45] Perrot, E.; Humbert, A.; Piednoir, A.; Chapon, C.; Henry, C. R. STM and TEM studies of a model catalyst: Pd/MoS_2(0001). *Surf. Sci.* **2000**, *445*, 407–419.

[46] Kresse, G.; Joubert, D. From ultrasoft pseudopotentials to the projector augmented-wave method. *Phys. Rev. B* **1999**, *59*, 1758–1775.

[47] Perdew, J. P.; Burke, K.; Ernzerhof, M. Generalized gradient approximation made simple. *Phys. Rev. Lett.* **1996**, *77*, 3865–3868.

[48] Kresse, G.; Furthmüller, J. Efficient iterative schemes for *ab initio* total-energy calculations using a plane-wave basis set. *Phys. Rev. B* **1996**, *54*, 11169–11186.